
Article:
Bugryniec, P., Davidson, J. and Brown, S. (2020) Advanced abuse modelling of Li-ion Cells – A novel description of cell pressurisation and simmering reactions. Journal of Power Sources, 474. 228396. ISSN: 0378-7753

https://doi.org/10.1016/j.jpowsour.2020.228396

Advanced Abuse Modelling of Li-ion Cells – A Novel Description of Cell Pressurisation and Simmering Reactions

Peter J. Bugryniec[a], Dr Jonathan N. Davidson[b], Dr Solomon F. Brown[a,*]

[a]*Department of Chemical & Biological Engineering, University of Sheffield, Sheffield, S1 3JD, UK*
[b]*Department of Electronic & Electrical Engineering, University of Sheffield, Sheffield, S1 3JD, UK*

Abstract

Thermal runaway (TR) is a significant safety concern for Li-ion batteries (LIBs), which, through computational modelling can be better understood. However, TR models for LIBs lack a proper representation of the build-up of pressure inside a cell under abuse, which is integral to predicting cell venting. Here, an advanced abuse model (AAM) is developed and compared to a classical TR model, considering a lithium iron phosphate (LFP) cell case study. The AAM accounts for two additional features: 1) venting, with a novel description of the internal cell pressure governed by the bubble point of the electrolyte/decomposition-gas mixture, and 2) simmering reactions. The novel bubble pressure assumption is validated against experimental data, and we show that the AAM significantly improves the predictions of time to TR and of temperatures after TR. Further, it is shown that there is significant uncertainty in the parameters defining the decomposition reactions for LFP cells. Importantly, cell pressurisation is most dependent on the gases released by the solid electrolyte interphase reaction, and venting is dependent on cell burst pressure and reaction activation energies. The AAM is essential for accurate abuse modelling, due to its improved temperature predictions, and considerably enhances the LIB TR field of study.

Keywords: Thermal Runaway, Lithium-ion, Lithium Iron Phosphate, Vessel Depressurisation, Gas Venting, Bubble Pressure

1. Introduction

Lithium-ion (Li-ion) batteries (LIBs), because of their superior performance compared to other batteries [1, 2], are at the forefront of electrochemical energy storage. Due to the safety concerns related to LIBs, viz. thermal runaway (TR) and the fires they can cause [3–5], cells are designed to pass several compulsory test standards [6, 7]. However, even with these standards in place, TR of LIBs still occurs [8–11]. Even lithium iron phosphate (LFP) cells, which have been shown to be the safest Li-ion chemistry [12–14], have been reported to have TR incidents [15].

*Corresponding author
Email address: s.f.brown@sheffield.ac.uk (Dr Solomon F. Brown)

Experimental investigations [16–18] are important to understanding cell safety [19]. However, in contrast with computational modelling, the financial and time cost of experimentally investigating large battery systems can be prohibitive. Hence, battery safety models are beneficial, but first require an accurate and validated model of the TR behaviour of a single cell.

Many TR models for Li-ion cells of different chemistries (e.g. LCO [20–23], LFP [23–25]; and NCA, LMO, NMC [23]) and under various abuse conditions (e.g. oven exposure [20–22, 24], accelerated rate calorimetry (ARC) [26], short circuit [27] and nail penetration [28]) have been developed. However, the existing TR models developed for LFP cells are either inaccurate [24], or have not be validated [23] and have been shown to be inaccurate when compared to recent experimental work by Ref. [29]. Inherently, the confidence in the parameter values used in LFP abuse models is low. Especially considering such models [23, 24] use values for reaction kinetics determined for LCO cells [20], which Abada *et al.* [25] shows to be, in part, inappropriate for LFP cells as the activation energies and active material specific content have to fitted to experimental work. Further, while Abada *et al.* [25] validate their model, it is to a low accuracy, and it further lacks any determination of the cell venting.

TR is a process where the heat generated from the exothermic chemical decomposition of a Li-ion cell's components leads to an uncontrollable temperature rise, that can eventually lead to the cell catching fire and/or exploding [3, 30]. Additionally, the decomposition of the cells' components leads to gas generation, cell pressurisation and, eventually, venting of flammable gases when the cells' internal pressure reaches the safety vents' burst cap pressure limit [31–33].

Typically the decomposition reactions considered in TR modelling which lead to heat generation are: (1) solid electrolyte interphase (SEI) reaction; (2) negative-solvent (NE) reaction; (3) positive-solvent (PE) reaction; (4) electrolyte decomposition (see for example [26, 30]). The typical temperature ranges at which the decomposition reactions begin, and the temperature at which the peak reaction rates occur, are listed in Table 1, while Table 2 lists the heats of reaction for the electrode reactions. Reactions involving the binder are deemed insignificant by [26], and, as such, are not typically accounted for in the literature [22, 23, 27]. Electro-chemical behaviour has been modelled [34–36], which allows the determination of (ir)reversible heat generation from battery operation. The heat generation by internal short when the separator melts has also been considered [37]. Cell pressurisation and heat lost due to venting have been considered by [33, 38], where it was found that these are important features to considerer for accurate predictions of TR, and hence are included in the AAM.

The widely adopted approach to modelling TR in Li-ion cells is to represent the individual decomposition reactions by separate Arrhenius expressions [21, 26, 41, 52]. A broad range of literature has shown that this method is suitable for simulating TR under different conditions [20–24, 27, 34, 37, 53, 54], and allowing for the analysis of the reactions

Table 1: Key Temperatures relating to decomposition reactions

Reaction	Self-heating onset temperature °C	Temperature at peak temperature rate °C	Reference
SEI	50–120	253–300	[39, 40]
NE	80–160	200–350	[39, 41–44]
PE	180–250	210–360	[13, 45–48]
Electrolyte	>250	-	[49]

Table 2: Range of heats of reaction for cell decomposition reactions.

Reaction	Heat released, ΔH ($J\,g^{-1}$)	Reference
SEI	112–578	[21, 34, 35, 50]
NE	1300-2800	[39, 43, 51]
PE	150–340	[45, 47, 49, 51]
Electrolyte	155–645	[26, 35, 37]

contributing to TR.

As cell pressurisation and gas venting can occur throughout TR [16], it is important to consider pressurisation in abuse models. Phase changes and mass losses during the venting process will carry energy away from the cell and in turn affect the temperature of the cell [33]. The calculation of the internal cell pressure during TR has been carried out by summing the saturation pressure of the electrolyte and the pressure of the decomposition gases determined by the ideal gas law [38]. However, calculating the pressure of a multiphase (liquid and vapour), multi component (e.g. electrolyte and decomposition gases) fluid is more commonly done under the bubble point assumption [55].

Reaction kinetic parameters can be determined through numerical analysis of thermal abuse experiments [35, 41, 42, 50, 56], namely ARC and differential scanning calorimetry (DSC) [57]. To ensure the kinetic parameters are independent of experimental method and valid over a wide range of scenarios these methods require multiple samples [50, 56, 58–60].

Computational parameter estimation requires fewer sample data sets as an objective, and thus provides the opportunity for simpler and more accessible abuse model development. However, parameterising TR models is difficult due to the reactions: having non-unique parameters; been non-linear; and having complex interaction between parameters [41, 42, 59, 60]. To address some of these difficulties Gaussian Processes and Global Sensitivity Analysis techniques have also been employed to determine kinetic parameters of a TR model [61], but this is currently outperformed by heuristic parameter fitting.

Determining the reaction kinetics for individual reactions leads to the overall model having discrepancies at validation [21, 22, 24, 50]. However, determining the kinetic parameters of a whole cell leads to acceptable results, but can lead to loss of information by not taking account of venting [33]. The amount of energy that is dissipated by venting

can be significant, while inclusion of venting improves overall model predictions [33, 38].

The aim of this paper is to develop an extended TR abuse model, referred to as the advanced abuse model (AAM), and validate it for LFP cells. Within this, the objectives are to: 1) determine appropriate set(s) of abuse parameters of LFP abuse models, 2) improve the accuracy of predictions by including novel descriptions of cell pressurisation, venting and simmering reactions, and 3) investigate their effect on model parameterisation. From this, we make the following novel contributions:

(1) highlighting the caution that should be taken when using parameter values quoted in the literature for the reaction kinetics;

(2) developing a novel methodology for the calculation of the internal cell pressure for more accurate venting predictions;

(3) investigating the effect of reaction parameters on cell venting;

(4) developing a novel methodology for modelling the simmering reaction of LFP cells; and

(5) discussing the effect of including the venting and simmering behaviour on determination of reaction kinetic parameter values.

This work is organised as follows: Section 2 presents the methodology of the AAM, including the individual sub-models it is constructed from, and, how they are coupled and applied over the model geometry; Section 3 presents the results and discussion, including preliminary work on the effects of assumed mass composition on parameterisation of the model, validation of the novel methodology for predicting the internal cell pressure, and, following this, an assessment of the AAM against experiential data and classical TR model results. Finally, Section 4 concludes the work, highlighting cautions that should be taken in TR model development, outlining the improvements the AAM has over the classical model, and summarizing the link between reaction parameters and venting behaviour.

2. Methodology

The governing equations of the Li-ion cell abuse model are organised into several sub-models that describe the heat-transfer, decomposition heat generation and venting behaviours, as illustrated in Fig. 1(a), applied over the model geometry shown in Fig. 1(b). The heat-transfer sub-model considers general conduction, convection and radiation terms for a solid body, with additional heat source terms coupled from the abuse and venting sub-models. The abuse sub-model describes the most commonly considered exothermic decomposition TR reactions, viz. the SEI, NE, PE and electrolyte reactions [20, 21, 37]. Further, the LFP cell under study is observed to generate heat through a simmering reaction, see Section 2.1.1. The abuse model is extended to include this additional heat generation

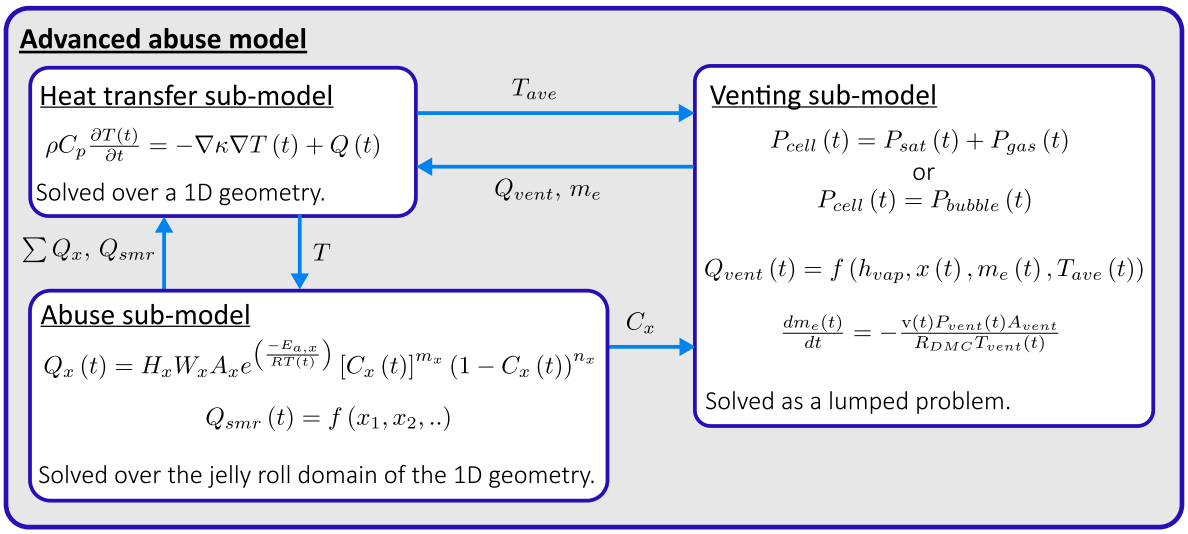

(a)

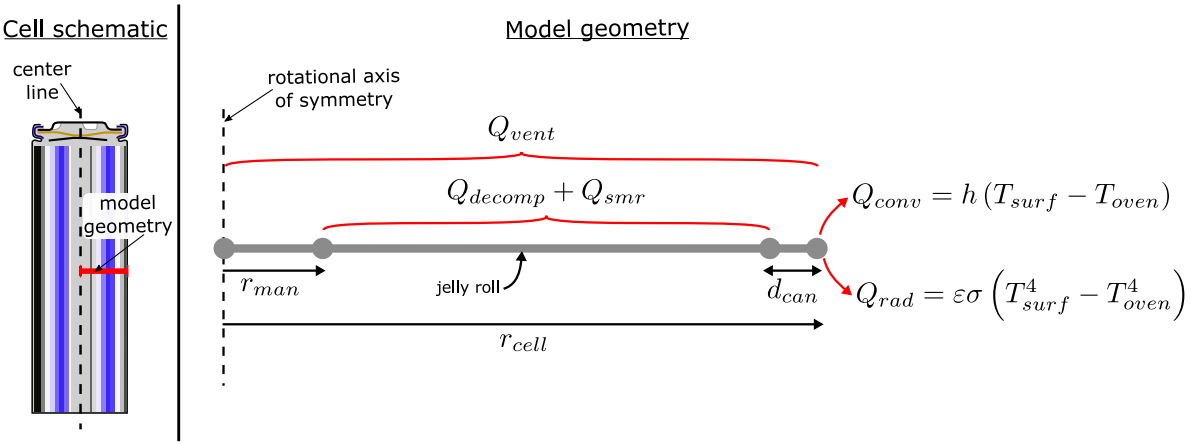

(b)

Figure 1: Model design. (a) Coupling of sub-models within the advanced abuse model (b) model geometry.

term. The venting sub-model describes the internal cell pressure and the heat lost upon venting. It is formulated to take account of the CO_2/DMC mixture, and its phase change upon boiling, by assuming it occurs in thermodynamic equilibrium at the mixture's bubble point. The governing equations for the abuse and venting sub models are discussed in further detail below, see Section 2.1 and Section 2.2 respectively, while the heat transfer sub-model is omitted as it is only dependent on fundamental thermal diffusion and energy balance theory.

2.1. Abuse Sub-Model

The governing equations for the decomposition reactions are those used commonly in the literature [20, 21, 37], and, for brevity, are not reproduced here. Instead, a brief description is given while the reader is directed to Ref. [20] for an unabridged explanation. With reference to the abuse sub-model in Fig. 1(a), showing a general reaction x, the

rate of reactions, R_x (s^{-1}), for reactions $x = \{sei, ne, pe, ele\}$ are described by individual Arrhenius reactions. The Arrhenius reactions are functions of the frequency factor, A_x (s^{-1}), the activation energy, $E_{a,x}$ (J mol^{-1}), temperature, T (K), the ideal gas constant, R (8.3145 J mol^{-1} K^{-1}), and the dimensionless quantities of reaction species, C_x , and constants n_x and m_x . The change in reaction species is governed by the reaction rate, while the heat generated by each reaction Q_x (W m^{-3}) is the product of the specific heat of reaction, H_x (J kg^{-1}), the volume specific content, W_x (kg m^{-3}) and the reaction rate. The total decomposition heat, Q_{decomp}, is equal to the sum of the four decomposition heats.

2.1.1. Simmering Reaction

The cells under study in this work are observed to undergo steady state reactions after the main TR event, leading to a cell temperature above the oven temperature at very large times after TR [29]. Here this is referred to as the "simmering reaction". We attribute this to a slow unknown reaction or reactions, due to rate limiting factors (species and oxygen availability) and a lack of concentration dependency. As such, the simmering reaction can then be assumed to be a zero-order reaction [62]. Due to the unknown nature of the simmering reaction, i.e. the reactive pathways/species and rate limiting factors, quantifying the parameters of the Arrhenius function is difficult. Hence, to account for the simmering reaction, Q_{smr} (W m^{-3}), of the LFP cell, and in turn investigate its effect on model predictions, a formulation that can be simply parameterised is developed:

$$Q_{smr} = \begin{cases} 0 & \text{before venting} \\ Q_{smr}^{max} \frac{T_{ave}-T_1}{T_2-T_1} t_{smr} & \text{at and after the point of venting} \end{cases} \tag{1}$$

Eq. (1) has no heat generation before venting. After venting, the simmering reaction is assumed to have linear behaviour as a function of temperature, $T_1 \leq T_{ave} \leq T_2$, and time, t_{smr}. The temperature bounds T_1 and T_2, determined by fitting, are implemented such that, during the main TR event, the simmering reaction is restricted to emulate the limited availability of reaction species and oxygen.

The term t_{smr} is the normalised length of time that the simmering reaction goes on for and is defined by Eq. (2).

$$t_{smr} = max\left(\frac{t_{smr,length} - (t - t_{vent})}{t_{smr,length}}, 0\right) \tag{2}$$

t_{smr} linearly reduces from 1 to 0 over the time interval $t_{smr,length}$. In Eq. (2), t is the simulation time parameter and t_{vent} (s) is the time at which venting occurs. $t_{smr,length}$ is estimated in order to fit the temperature gradient of the cell under oven simulation long after the main TR event.

Through fitting, the parameters of Eq. (1) and Eq. (2) were determined to be $Q_{smr}^{max} = 85\,\mathrm{kW\,m^{-3}}$, $T_1 = 120$°C

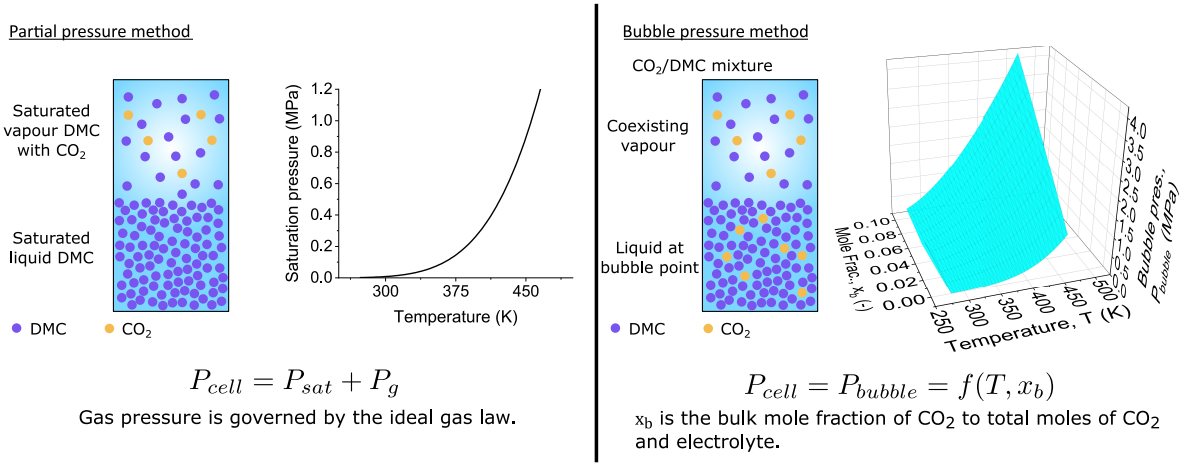

Figure 2: Comparison of theory behind venting sub-model methodologies.

and $T_2 = 218°\text{C}$, while $t_{smr,length} = 600\,\text{min}$ was estimated.

2.2. *Venting Sub-Model*

The internal cell pressure is determined by the bubble point venting (BPV) method, developed in this work, that calculates the bubble point pressure of the CO_2/DMC mixture. The partial pressure venting (PPV) method, which reproduces work by Coman *et al.* [38], is used for comparison. An overview and comparison of these methods is shown in Fig. 2.

The PPV method accounts for the heat and mass loss due to expulsion of electrolyte and decomposition gases from a Li-ion 18650 cell. For conciseness, only a description of the governing theory is given here, along with equations that are significant in relation to the development of the updated venting sub-model. The venting sub-model describes the energy and mass balance for an unsteady flow in an open system. The mass loss is described by the loss of electrolyte through the vent at the point at which the vent opens, i.e. when the internal cell pressure is greater than the vent burst disc pressure limit. The mass loss through the vent is assumed to be isentropic, wherefore the vented electrolyte mixture behaves as an ideal gas passing through a nozzle. The internal cell pressure is, in the literature [38], a sum of the partial pressure of the saturation pressure of the DMC electrolyte and the pressure of the generated decomposition gases. The pressure is calculated from the ideal gas law using the mass of gas generated. The generation of gas is governed by the SEI reaction rate from the abuse sub-model, while its loss is governed by the mass loss rate of electrolyte. However, here, in the development of the AAM, an averaged and normalised reaction rate of all reactions is used (see Eq. (3)) such that the importance of individual reactions on gas generation and venting can be determined. Although it is known that secondary and interdependent reactions occur during TR [63], here for simplicity and compatibility with typical TR modelling [e.g 23], the gas generation governed by Eq. (3) is only

dependent on the primary (SEI, NE, PE and electrolyte) reactions. Further, as the formulation of Eq. (3) implies equal weighting of reactions to the overall decomposition of the cell, then, inherently, the maximum amount of gas produced is equally split over the four reactions.

$$C_{rxn} = \frac{\frac{C_{sei}}{C_{sei,0}} + \frac{C_{ne}}{C_{ne,0}} + \frac{1-C_{pe}}{1-C_{pe,0}} + \frac{C_e}{C_{e,0}}}{4} \tag{3}$$

In both the PPV and BPV methods, the liquid-vapour mixture occupies a constant volume, considering the rigid body of the cell. Further, the following assumptions are made about the flow of gas from the cell upon venting [38]: the liquid and vapour phases are incompressible, and the gas and vapour phases follow ideal gas behaviour during venting. The energy contribution from the gas phase is neglected as the amount of gas is small. Even though the electrolyte is a multi-component liquid, only the DMC component is considered. Finally, no solid mass is ejected.

2.2.1. Coupling of the Sub-Models

The 0D venting sub-model must be appropriately coupled to the 1D heat transfer sub-model to account for the mass, heat capacity and density changes, and their effects on the thermal capacity of the cell and the electrolyte reaction specific mass. The total mass of electrolyte in the cell, m_e^*, accounting for mass loss, is given as:

$$m_e^* = m_e^0 - m_{e,vent}^0 + m_{e,vent} \tag{4}$$

where m_e^0 is the total initial mass of electrolyte in the cell, $m_{e,vent}^0$ is the amount of electrolyte estimated to be ejected upon venting, and $m_{e,vent}$ is the amount of electrolyte ejected as a function of time. At $t = 0$, $m_{e,vent} = m_{e,vent}^0$. At venting, the model predicts total loss of $m_{e,vent}^0$, so the value of $m_{e,vent}^0$ is fitted such that the model predicts a magnitude of temperature drop upon venting comparable to that observed in the experimental data. The change in $m_{e,vent}$ is determined by:

$$\frac{dm_{e,vent}}{dt} = -\frac{\mathrm{v} P_{vent} A_{vent}}{R_{DMC} T_{vent}} \tag{5}$$

where v, P_{vent} and T_{vent} are the velocity, pressure and temperature of the vent gases, respectively, A_{vent} is the area of the vent opening and R_{DMC} is the specific gas constant of DMC.

From the energy balance equation in [38], two relationships can be defined such that the 0D venting sub-model can be coupled to the heat transfer-abuse model. These are the heat loss during venting Q_{vent}:

$$Q_{vent} = -m_e^* \frac{dx}{dt} h_{vap} - h_{vap} \frac{dm_e^*}{dt} (x - 1) \tag{6}$$

and the change in cell heat capacity $m_{cell}C_{p,cell}$:

$$m_{cell}C_{p,cell} = m_s C_{p,s} + m_e^* \left[(1-x)\, C_{p,l} + x C_{p,v}\right] \tag{7}$$

where h_{vap} and x are the heat of vaporisation and mole fraction of the DMC, respectively. $C_{p,s}$, $C_{p,l}$ and $C_{p,v}$ are the specific heat capacities of the solid components, liquid electrolyte and electrolyte vapour, respectively.

If the average cell properties m_{cell} and $C_{p,cell}$, the physical properties for the DMC electrolyte and the electrolyte mass are known, then relations to estimate the mass and specific heat capacity of the solid components can be defined. The mass of solid components can be determined from:

$$m_{cell} = m_s + m_e^* \tag{8}$$

where the constant m_s can be determined from the initial measured cell mass m_{cell} and the initial mass of electrolyte m_e^0.

Similarly, the specific heat of the non-electrolyte components, can be estimated from Eq. (7) by rearranging for $C_{p,s}$ and substituting in relevant initial values, assuming that $C_{p,s}$ is constant with temperature. With m_s and $C_{p,s}$ known, relevant time-varying physical properties, i.e. density $\rho_{cell,t}$ and specific heat $C_{p,cell,t}$, for the cell can be defined by:

$$\rho_{cell,t} = \frac{m_s + m_e^*}{V_{cell}} \tag{9}$$

and

$$C_{p,cell,t} = \frac{m_s C_{p,s} + A}{m_s + m_e^*} \tag{10}$$

$$A = \begin{cases} m_e^* \left[(1-x)\, C_{p,l} + x C_{p,v}\right] & \text{before venting} \\ (m_e^0 - m_{e,vent}^0) C_{p,l}^{DMC} & \text{after venting} \end{cases} \tag{11}$$

where V_{cell} is the volume of the cell. The time varying specific heat of the cell (Eq. (10)), takes two forms: one for before venting and one for after. After venting, the remaining electrolyte is assumed, for simplicity, to be completely in the liquid phase. This is a significant assumption; however, the properties (phase and vapour fraction) of the DMC after venting are hard to predict because the liquid-vapour data for the DMC electrolyte is only defined up to temperatures of 327°C, below the maximum cell temperature observed experimentally, 400°C, (see Ref. [29]). Also, at atmospheric pressure and TR temperatures (i.e. assumed cell properties after venting) the DMC would be in the gas phase [64]. However, prediction of the transition from liquid to gas is difficult and beyond the scope of this work.

Finally, as the abuse model is dependent on mass of reactants, i.e. m_e, the specific mass of electrolyte is replaced by:

$$W_e = \frac{m_e}{V_{jelly}} \tag{12}$$

where V_{jelly} is the jelly roll volume.

2.2.2. Venting-Sub Model Development: Bubble Pressure

The BPV method is developed to account for the correct phase equilibria of the CO_2/DMC system, rather than assume an ideal mixture of an ideal gas and a saturated liquid. The BPV method is governed by the mole fraction x_b, which is the bulk ratio of moles of CO_2 to total moles of the CO_2/DMC mixture (see Eq. (14)), while the vapour-liquid fraction is not calculated. This is to avoid iteratively determining the vapour-liquid fraction and mole fraction of each component in each phase, as this would be slow to calculate and beyond the scope of this work. As such, the vapour properties are neglected from the BPV method as the amount of vapour is assumed small and has negligible effect on the thermo-physical properties. Hence, fluid parameters (i.e. the heat of vaporisation $h_{vap,b}$, specific heat of the liquid phase $C_{p,l}^{mix}$ and internal cell pressure P_{bubble}) are redefined for the CO_2/DMC mixture in terms of temperature, T and x_b.

The properties (P_{bubble}, $C_{p,l}^{mix}$ and $h_{vap,b}$) were determined from the commercial software *REFPROP - NIST Standard Reference Database* [64]. These parameters were defined in the range of 0°C to 187°C and for various liquid phase mole fraction ratios from 0.0001:0.9999 to 0.1:0.9 (CO_2:DMC). The temperature range is such that it covers cell temperatures from ambient up to the venting temperature (175°C [29]), at which point the bubble pressure assumption is no longer valid. Expressions, that are executable within *COMSOL*, for P_{bubble}, $C_{p,l}^{mix}$ and $h_{vap,b}$ are fitted to the *REFPROP* data, minimising the root mean squared error (RMSE) of the surface polynomial.

In the manner described above, the bubble pressure and internal cell pressure, is determined to be:

$$\begin{aligned} P_{bubble} = {} & 5.652 - 3.531{\times}10^{-2}T - 42.38x_b + 5.495{\times}10^{-5}T^2 \\ & + 0.1643Tx_b - 11.56x_b^2 \end{aligned} \tag{13}$$

where T is temperature and x_b is the mole fraction:

$$x_b = \frac{\frac{m_g}{M_g}}{\frac{m_g}{M_g} + \frac{m_e^*}{M_{DMC}}} \tag{14}$$

where m_e^* is described by Eq. (4), m_g is the mass of gas, and M_{DMC} and M_g are the molar masses of the DMC electrolyte and (CO_2) gas respectively. The initial amount of gas in the BPV method, to determine the initial mole

fraction x_b^0, is set to be the same as used in the PPV method [38] for a fair comparison between methods.

The heat of vaporisation of the CO_2/DMC mixture is not given by *REFPROP* [64]. However, the isobaric heat of finite vaporisation can be estimated from the integral of the isobaric heat of infinitesimal vaporisation, q_P, as described by [65]. This can be summarised as the estimated heat of total vaporisation of a fluid at the bubble point ($\omega_a = 0$) to a fluid at the dew point ($\omega_b = 1$), and can be determined from the difference in vapour and liquid enthalpies at constant pressure:

$$\begin{aligned} h_{vap,est} &= \frac{h(P,1) - h(P,0)}{1-0} \\ &= h_v(P) - h_l(P) \end{aligned} \tag{15}$$

From this, a function of the heat of vaporisation, $h_{vap,b}$, can be determined from the liquid a vapour enthalpies of the mixture over the temperature and molar fraction ranges defined above:

$$h_{vap,b}(T, x_b) = \sum_{i=0}^{4} \sum_{j=0}^{4} a_{i,j} T^i x_b^j \tag{16}$$

where the coefficients $a_{i,j}$ are given by Eq. (17).

$$a_{i,j} = \begin{pmatrix} 365.2 & 2.091\times10^{4} & -6.206\times10^{5} & 5.114\times10^{6} & -1.128\times10^{7} \\ 2.917 & -7.097 & 911.4 & -6355 & 0 \\ -1.359\times10^{-2} & -6.391\times10^{-2} & 3.152\times10^{-1} & 0 & 0 \\ 1.799\times10^{-5} & -1.194\times10^{-5} & 0 & 0 & 0 \\ -6.189\times10^{-9} & 0 & 0 & 0 & 0 \end{pmatrix} \tag{17}$$

The specific heat capacities for the liquid phase and vapour phase, utilised in Eq. (7) and Eq. (10) are replaced by:

$$\begin{aligned} C_{p,l}^{mix} = 2.111 &- 3.312\times10^{-3} T - 0.614 x_b + 7.959\times10^{-6} T^2 \\ &+ 2.031\times10^{-3} T x_b + 4.997\times10^{-1} x_b^2 \end{aligned} \tag{18}$$

The polynomials of P_{bubble}, $C_{p,l}^{mix}$ and $h_{vap,b}$ have R^2 and RMSE values as listed in Table 3, and show a high quality of fit.

With the newly defined properties of the mixture ($C_{p,l}^{mix}$ and $h_{vap,b}$), the heat lost due to venting, the average cell heat capacity and solid component heat capacity are redefined, from the PPV methodology, to be in line with the BPV

Table 3: Quality of Fit of P_{bubble}, $C_{p,l}^{mix}$ and $h_{vap,b}$ Functions.

	$\mathbf{P_{bubble}}$	$\mathbf{C_{p,l}^{mix}}$	$\mathbf{h_{vap,b}}$
R^2	0.9995	0.9993	0.9930
RMSE	0.0209	0.0038	8.4910

methodology. $C_{p,alt}$ is the alternative definition of cell heat capacity:

$$C_{p,alt} = \frac{(m_s C_{p,s}) + (A_b)}{m_s + m_e^*} \tag{19}$$

where A_b (see Eq. (20)) accounts for the heat capacity of the electrolyte.

$$A_b = \begin{cases} m_e^* C_{p,l}^{mix} & \text{before venting} \\ (m_e^0 - m_{e,vent}^0) C_{p,l}^{DMC} & \text{after venting} \end{cases} \tag{20}$$

A_b is a function of the liquid phase heat capacity of the mixture before venting, while, after venting, it is a function of the DMC heat capacity as a pure liquid.

The constant heat capacity of the solids, determined from the initial mass and heat capacities of the whole cell and electrolyte, is defined as:

$$C_{p,s} = \frac{m_{cell} C_{p,cell} - m_e^0 C_{p,l}^{mix}(T_{int}, x_b^0)}{m_s} \tag{21}$$

The heat of vaporisation, $h_{vap,b}$, is used in the determination of the venting cooling power:

$$Q_{vent,b} = h_{vap,b} \frac{dm_{mix}}{dt} \tag{22}$$

where m_{mix} is the total mass of electrolyte and gas mixture, given by Eq. (23), and $\frac{dm_{mix}}{dt}$ is only valid upon venting.

$$m_{mix} = m_e^* + m_g \tag{23}$$

2.3. Implementing Equations, Model Geometry and Parameter Estimation

The model was developed in the commercial finite element modelling software *COMSOL Multiphysics* [66]. The heat transfer sub-model is implemented using the relevant built-in equations within *COMSOL*. The reaction rates of the abuse sub-model are implemented through domain ODEs, while the mass rate of the venting sub-model is implemented by a global ODE.

The model geometry, see Fig. 1(b), represents an axi-symmetric, one dimensional slice through an 18650 cyl-

Table 4: General Parameters

Parameter	Value	Source/ notes
Specific heat capacity of cell, C_p (J kg^{-1} K^{-1})	1107	measured [29]
Thickness of cell can, d_{can} (mm)	0.3	[67]
Surface emissivity of cell, ε (-)	0.8	[21]
Convection coefficient, h_{conv} (W m^{-2} K^{-1})	12.5	[21]
Height of cell, h_{cell} (mm)	65	measured
Height of jelly roll, h_{jelly} (mm)	57.3	[67]
Radial conductivity of cell, κ (W m^{-1} K^{-1})	0.5	estimated
Mass of cell, m_{cell} (g)	39.9	measured
Radius of cell, r_{batt} (mm)	9	measured
Radius of mandrel, r_{man} (mm)	2	[67]
Density of cell, ρ (kg m^{-3})	2418	measured [29]
Initial cell temperature, T_{init} (°C)	16.5	See note[a]
Oven set temperature, T_{oven} (°C)	180, 218	See note[a]
Simulation length, t_{length} (min)	90	See note[a]
Abuse parameters		
Initial species concentration SEI, $C_{sei,0}$ (-)	0.15	[20]
Initial species concentration NE, $C_{ne,0}$ (-)	0.75	[20]
Initial SEI thickness, $t_{sei,0}$ (-)	0.33	[20]
Initial species concentration PE, $C_{pe,0}$ (-)	0.04	[20]
Initial species concentration E, $C_{e,0}$ (-)	1	[20]
m_{sei} (-)	1	[20]
n_{sei} (-)	0	[20]
m_{ne} (-)	1	[20]
n_{ne} (-)	0	[20]
m_{pe} (-)	1	[20]
n_{pe} (-)	1	[20]
m_{ele} (-)	1	[20]
n_{ele} (-)	0	[20]

[a]set to match experimental conditions.

indrical cell. The heat transfer equations are applied over the entire cell geometry, while the decomposition reactions and simmering reaction are applied over the jelly roll domain. The venting sub-model is solved through a coupled 0D component, see Fig. 1(a), from which the heat loss due to venting is determined and applied over the entire cell geometry.

Throughout this work the cells' thermo-physical and heat transfer properties, as well as the initial values of the dependent variable within the decomposition reactions and the constants m_x and n_x, are kept the same between investigations. These general parameters are given in Table 4.

The model is developed against experimental data of LFP 18650 (1.5 Ah) cells under oven exposure, from our previous work [29]. Parameter estimation is carried out, using heuristic fitting methods, in search of appropriate parameter values because preliminary studies using literature values (from [23]) are inaccurate (as discussed in Section 3.1). Reactions are progressively introduced to the model, and their parameters estimated, as the model is fitted

to a larger proportion of the experimental data.

3. Results and Discussion

3.1. Preliminary Findings - Using the Classical Abuse Model

Preliminary oven abuse simulations were carried out using literature decomposition reaction parameters (see initial values in Table 5 and Table 6). The simulation results, presented in Fig. 3(a), are compared to experimental data from [29]. It can be clearly seen that the simulation vastly over-predicts TR severity while under predicting time to TR. From this, the high TR temperatures suggests that the heat within this reaction model is too large. I.e. the specific mass of reactant(s) or the heat of reaction(s) are too large. Further, the early occurrence of TR suggests the onset of (at least some of) the reactions occur at too low a temperature, i.e. the activation energies are, in general, too low. Hence, the reaction parameters ($E_{a,x}$, A_x, W_x and H_x) are of interest of investigation to determine appropriate values.

Abada *et al.* [25] has shown the importance of the values of specific masses. The specific mass of a jelly roll component can be derived from the mass of a given component within a cell divided by the jelly roll volume, V_{jelly} (here this takes a value of $V_{\text{jelly}} = 1.29 \times 10^{-5}$ m^3, calculated from Eq. (24)). The mass composition of LFP 18650 cells [31, 68] are presented in Table 7. The relative masses from Table 7 allow for the estimation of two compositions of the cells studied here (also presented in Table 7), providing two case studies, referred to as Cell A and Cell B. Cell A is derived from the mass ratios of [31], while Cell B is derived from the mass ratios of [68]. The calculated respective specific masses for each component in each case are presented in Table 8.

$$V_{jelly} = \pi h_{jelly} \left((r_{batt} - d_{can})^2 - r_{mandrel}^2 \right) \tag{24}$$

With the specific masses set to those from Table 8, parameter estimation on the abuse parameters ($E_{a,x}$, A_x and H_x) was carried out using the classical TR model. Following this procedure, the resulting prediction of cells undergoing TR during oven testing is presented in Fig. 3(b) and Fig. 3(c), for case A and B respectively.

From the results presented in Fig. 3(b) and Fig. 3(c), it can be seen the severity of TR has been be predicted accurately, significantly improving predictions over those using the initial values from Table 5. However, the shape of the temperature profiles differ in agreement with the experimental data depending on the oven set temperature. For both cases A and B, at the higher oven temperature, the cell surface temperature profile resembles that of the experimental data well. For the lower oven temperature case, while the peak temperature is predicted accurately, the smooth temperature profile is not reproduced. At the higher oven temperature, without the occurrence of venting (investigated in Section 3.2) the TR incident occurs sooner than that in the experiment. For each oven temperature, the model does not simulate any simmering reactions (investigated in Section 3.3), causing the discrepancies at later

Table 5: Abuse parameters for LFP cell, from literature and estimated parameters in terms of a factor of original value, used in preliminary studies.

Parameter	Absolute value Initial Case (from [23])	Scaling factor Case A	Case B
E_{a_ne} ($J\,mol^{-1}$)	1.3508×10^5	1.05	1.06
E_{a_sei} ($J\,mol^{-1}$)	1.3508×10^5	1.1	1.115
E_{a_pe} ($J\,mol^{-1}$)	1.03×10^5	0.935	0.965
E_{a_e} ($J\,mol^{-1}$)	2.74×10^5	1.1	1.05
A_{ne} (s^{-1})	2.5×10^{13}	1.0	1.0
A_{sei} (s^{-1})	1.667×10^{15}	1.0	1.0
A_{pe} (s^{-1})	2×10^8	1.0	1.0
A_e (s^{-1})	5.14×10^{25}	1.0	1.0
H_{ne} ($J\,g^{-1}$)	1714	2.0	1.65
H_{sei} ($J\,g^{-1}$)	257	2.249	2.249
H_{pe} ($J\,g^{-1}$)	194.7	1.24	1.0
H_e ($J\,g^{-1}$)	155	2.2	1.9

Table 6: Range of specific masses used in the modelling of TR (PE specifically for LFP cells), values used by [23] and the initial simulation here, and estimated values for better prediction of TR severity. [a]From references [20, 23, 26, 30, 36].

Specific Mass	Range[a]	Initial Values
W_{ne} ($kg\,m^{-3}$)	610-1700	1700
W_{pe} ($kg\,m^{-3}$)	960	960
W_e ($kg\,m^{-3}$)	407-500	500

Table 7: Cell composition by mass from literature and estimates for the cell under study

	Ref. [31]		Ref. [68]		Estimates for cell under study	
Capacity (Ah)	1.1		n/a		1.5	
	g	%	g	%	Cell A (g)	Cell B (g)
Cell Total	38.87		45.00		39.90	39.90
Cathode, active	7.73	19.90	14.22	31.60	7.94	12.61
Cathode, other	1.93	4.97	1.94	4.31	1.98	1.72
Anode, active	4.84	12.46	8.15	18.11	4.97	7.23
Anode, other	0.34	0.88	0.90	2.00	0.35	0.80
Electrolyte	6.41	16.50	2.20	4.89	6.58	1.95
Separator	1.15	2.96	2.00	4.44	1.18	1.77
Case	10.45	26.90	10.09	22.42	10.73	8.95
Foil	6.00	15.44	5.50	12.22	6.16	4.88

Table 8: Calculated specific masses for cell mass compositions of Case A and B.

	Case A		Case B	
	g	$kg\,m^{-3}$	g	$kg\,m^{-3}$
Anode, active	4.97	385	7.23	560
Cathode, active	7.94	615	12.61	977
Electrolyte	6.58	510	1.95	151

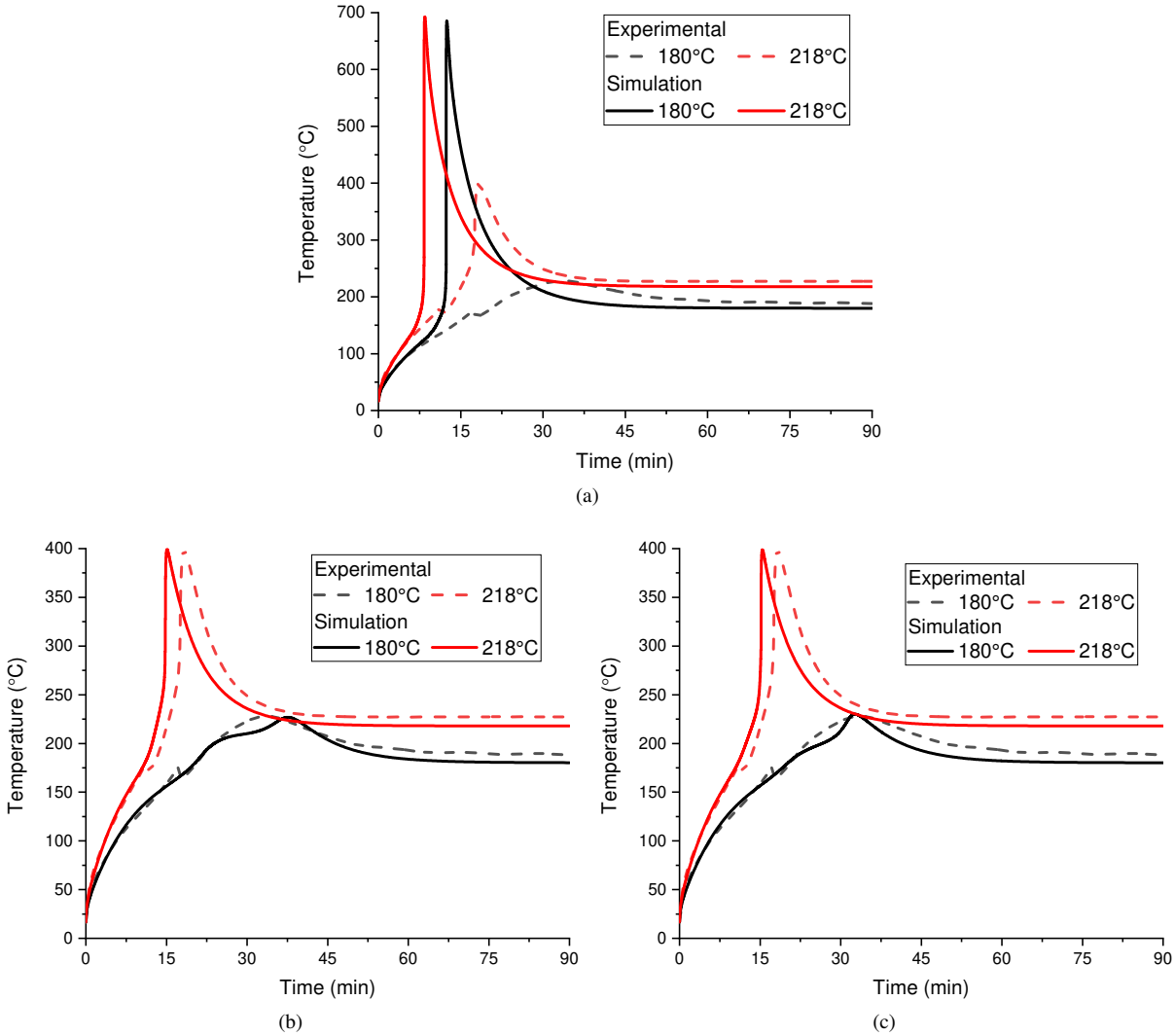

Figure 3: Preliminary results employing classical thermal runaway model simulating oven exposure and comparing to experimental results from [29]. (a) Using abuse parameters from [23] (see initial values Table 5 and Table 6); (b) and (c) fit of abuse parameters given the specific masses (of Table 8) for case A and B, respectively.

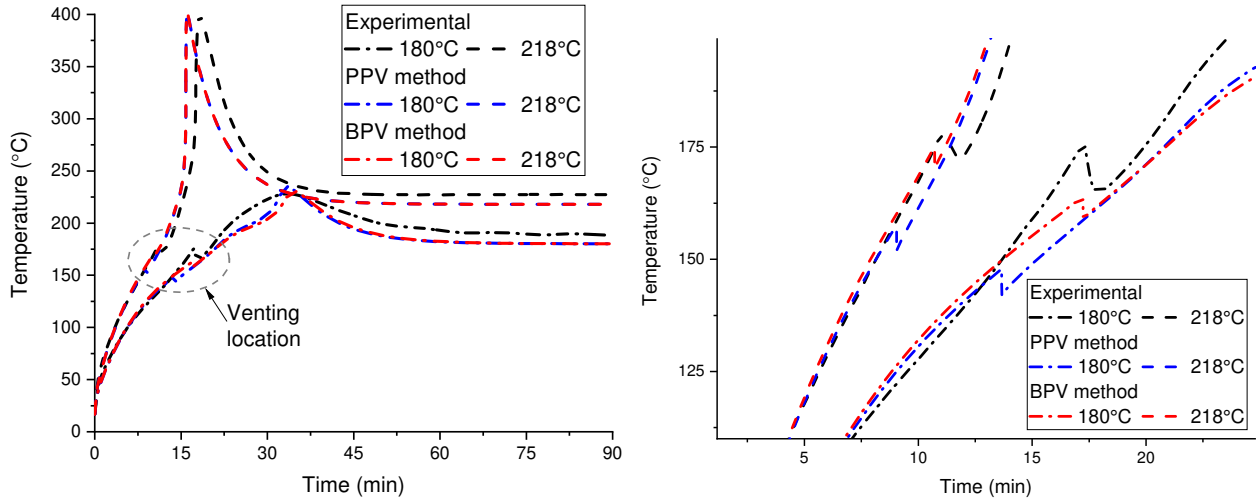

Figure 4: Oven abuse simulations for both internal pressure methods (a) whole time frame (b) enlargement of venting location.

times between the simulation and experimental results.

Table 5 presents the estimated parameters used to produce the predictions of Fig. 3(b) and Fig. 3(c). From this table, it is shown that to meet the TR maximum temperature the model requires significant changes to the heat of reactions.

3.2. Vent Sub-Model Development

A comparison between existing PPV and the new BPV methods is made. In both cases, the general properties from Table 4, the specific masses of cell A (Table 8), the abuse parameters corresponding to column A of Table 5 and a burst pressure (P_{burst}) of 1224 kPa are used.

Figure 4(a) shows the surface temperature of a cell under oven abuse simulations, at two oven set temperatures, using both venting methodologies, and compared to experimental results. The venting methodology has little effect on the overall predicted temperature profile and TR behaviour. The most significant difference between the methodologies is the temperature at which venting is predicted. As can be seen in Fig. 4(b), the BPV method predicts venting closer to the experimental data.

This can be further analysed by looking at the pressure vs surface temperature plots in Fig. 5(a). Firstly, it is important to note that, following the bubble point assumption, there should only exist a single electrolyte temperature for a given pressure and bulk mole fraction, this is not the case for the surface temperature. Unlike the PPV method, the BPV method predicts little pressure increase until approximately 110°C, at which point the pressure increases steeply. The sudden pressure increase in the BPV method simulation is because the cell is initially at a pressure of 0.1 MPa, which, for temperatures below 110°C and a mole fraction near the initial value, is greater than the bubble

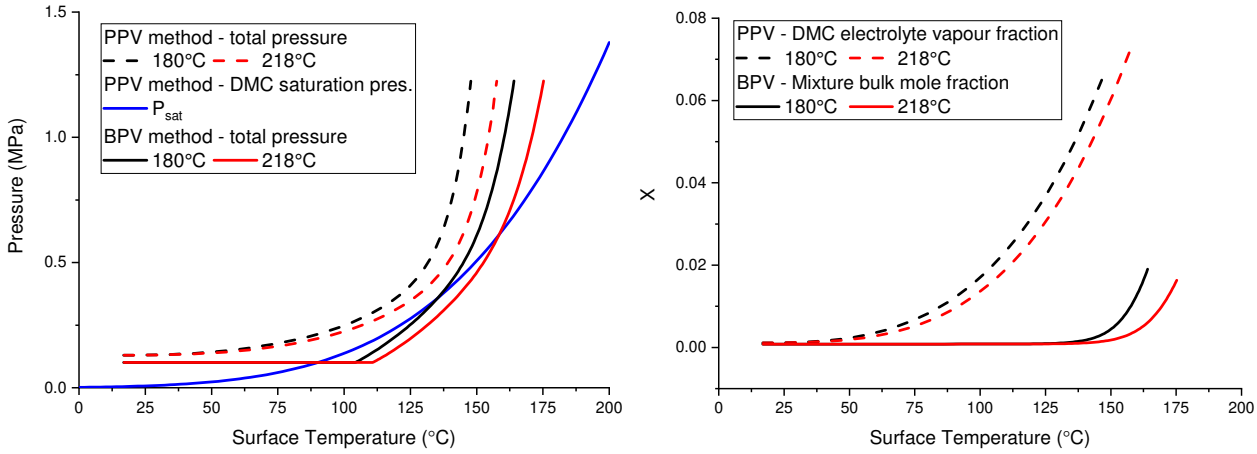

Figure 5: Comparison of (a) Pressure vs temperature (b) vapour or mixture fraction vs temperature, from oven abuse simulations for both internal pressure methods.

pressure. Hence, the pressure remains constant until temperatures greater than 110°C, at which point the bubble pressure is greater than 0.1 MPa and the pressure increases according to Eq. (14). Further, as the mole fraction remains relatively constant up to 125°C (see Fig. 5(b)), then the increase in pressure up to approximately 125°C is predominantly determined by temperature.

Although the pressure predictions at lower cell temperatures are significantly different between methods, once the mole fraction starts to increase, i.e. gas begins to be generated, then the pressure prediction of the BPV method resembles that of the PPV method, while somewhat offset along the temperature axis.

As stated above, there is a difference in the predicted temperature at which venting occurs between the two methods. However, one must consider that the literature, [38], fits the point of venting in simulations to experimental data by altering the SEI reaction activation energy. Hence, it is conceivable that either method could be used to predict venting in TR modelling, although each would require different reaction parameters to provide the same location of venting. However, the BPV method is, we believe, more representative of the system under study as it accounts for the phase equilibria of the mixture, unlike the PPV model which assumes the CO_2 generated is entirely in the gaseous phase. The BPV method will therefore be used in the remainder of this work.

Further, one can see in Fig. 4 that the BPV model predicts venting closer to the experimental data for the given parameters set. However, if the assumed burst pressure was to be higher (as in [69]) then the point of venting for both methods would be at a higher temperature. Hence, it can be clearly recognised that the assumed burst pressure can have an indirect influence on the abuse parameters through the need to accurately fit the location of venting. This will be systematically investigated as part of Section 3.3.

3.3. Advanced Abuse Model Investigation

This section discusses the results of the AAM, that includes the venting phenomena and simmering reactions, to address the suggested improvements in Section 3.1, along with a study of the effects of assumed burst pressure on abuse parameters.

Figure 6 shows the resulting temperature plots of oven simulations for the two different mass fractions (see Table 8) and for two different burst pressures. It can be clearly seen from Fig. 6(a) and Fig. 6(b) that the AAM predicts TR very accurately for the higher oven temperature exposure when compared to the experimental data, and vastly improves predictions when compared the classical abuse model, see Fig. 3(b) and Fig. 3(c). Specifically, the implementation of the venting behaviour delays TR noticeably, such that the peak temperatures of the simulation occur at a closer time to the experimental peak than the predictions of the classical model. Additionally, the shape of the temperature profile under lower oven temperature abuse scenario better resembles the experimental results using the AAM than when using the classical model.

From Fig. 6(a) and Fig. 6(b) it can be seen for the lower oven temperature exposure case the peak temperature and time to peak temperature are under predicted. Through the parameter estimation process it was found that to meet the peak temperature for the 180°C oven exposure case it was required that: 1) the heat of reaction of the NE reaction needed to be increased; or 2) the onset of the PE reaction to be lowered. However, either of these led to TR occurring to soon under the higher oven temperature exposure, while item 2 further lead to poor qualitative predictions for the lower temperature oven exposure. Hence, we suspect that there are secondary or interdependent reactions, such as SEI reformation/decomposition and/or secondary NE dependent reactions, that are most important to consider at lower oven exposure temperatures.

Inspection of the temperature profile upon venting shows that the predicted temperature drop occurs more rapidly than in the experimental data, see Fig. 6(c) and Fig. 6(d). Clearly, if the venting behaviour was predicted to occur more slowly, then the location of the peak temperature would be predicted more accurately. Hence, while the venting methodology used here significantly improves predictions, it also identifies that there are some important phenomena missing. It is hypothesised that this could be due to a disequilibrium between phases [70], as, upon venting of the vapour, there is a rapid pressure drop. When there is a pressure drop, for the liquid to remain in equilibrium, it must cool accordingly. If the liquid does not cool at a rate quickly enough for the pressure drop, this leads to superheated liquid, as has been seen elsewhere (see for example [71]). Equilibrium is re-established after some time as the liquid evaporates/ flashes, during which the depressurisation rate is reduced because the pressure starts to recover due to the volume increase of evaporation. Further, the inclusion of the simmering reaction improves the predictions after the TR event, showing its importance to the AAM.

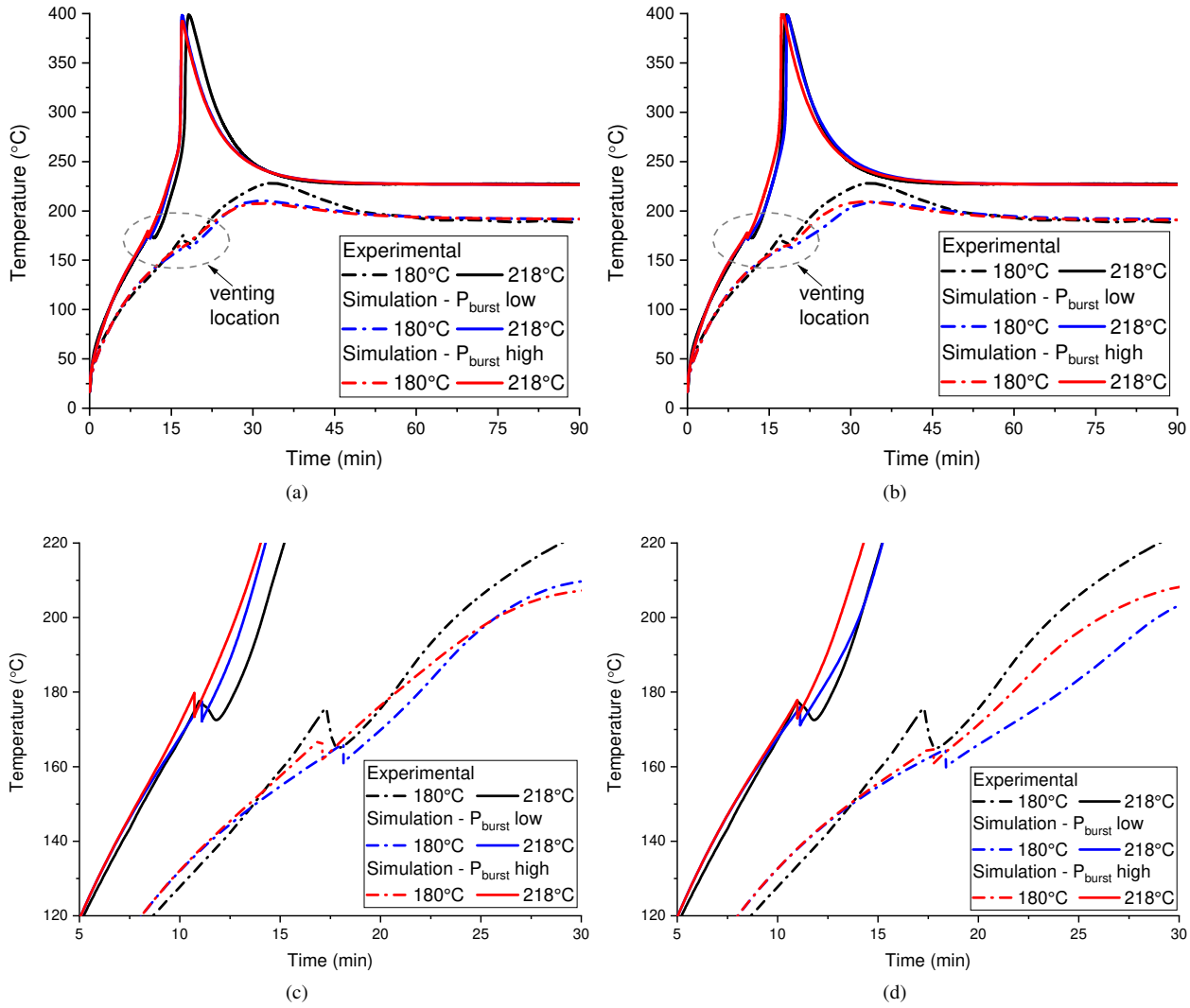

Figure 6: Temperature plots for oven abuse simulations for parametrised advanced abuse model (a) mass composition A (b) mass composition B (c) enlargement of venting location mass composition A and (d) enlargement of venting location mass composition B.

On inspection of the estimated parameters for the AAM (see Table 9) the values of the SEI, PE and electrolyte heats of reaction lie within the bounds presented in the literature (see Table 2). However, of most interest is the estimated values of the NE heat of reaction, which are larger than the upper bound. This is a direct result of the lower specific masses of carbon used in the AAM compared to the literature (see Tables 6 and 8), as the heat generated is directly related to the product of specific mass and heat of reaction for a given reaction. Also, for the case in which the specific mass of carbon is lowest, i.e. cases A, the value of H_{ne} is highest. Although the values of H_{ne} are relatively high (compared to the initial case), in case B the value is not significantly larger than the upper values found in the literature. As the value of H_{ne} is closer to literature bounds for simulations utilising mass composition B than A, this suggests that the mass ratio used in case B is a better representation of the mass composition of the cell under study.

The largest discrepancy is for the lower oven temperature case, see Fig. 6, where the PE reaction does not occur. Hence, improving the prediction at lower oven temperature and reducing the estimated value of H_{ne} could be addressed by the inclusion of additional reactions. With this, we suggest that other reaction(s), such as possible secondary and tertiary decomposition of active materials, decomposition of the reaction products and reactions involving the binder, should be accounted for, concurring with comments and findings made by [21] and [56].

Table 10 presents the heat generated by each reaction over the entire 90 min simulation and over the time only up to the point of maximum cell temperature. This table shows that the model predicts that, under the high oven temperature exposure, approximately 16 kJ of heat is produced, which is almost equal to the 17 kJ of electrochemically stored energy of the cell [29]. For the entire time period, most of this heat is produced by the NE reaction and the simmering reaction under both oven temperatures. However, up to the point of maximum cell temperature, it is the NE reaction that dominates the total heat generated, with a considerable contribution from the PE reaction at higher oven abuse temperatures.

Hence, for the LFP cell under study it can be said that TR is dominated by the heat from NE reaction, followed by the PE (at higher oven temperatures). After the maximum cell temperature, the heat generated is dominated by the simmering reaction followed by NE reaction, while for lower oven temperature the PE reaction contributes. As such, the greatest improvement to the safety of LFP cells can be made through cell developments that lead to a reduced heat of reaction of the NE reaction, for example, by electrolyte additives [72] or anode structure [73]. The heat lost through venting, while important to improve temperature predictions, is small in comparison to the total energy released before the maximum cell temperature.

3.3.1. Venting Behaviour

Returning to Fig. 6, the choice of burst pressure has little effect on overall TR predictions. However, venting is predicted to occur at slightly later times and lower temperatures for a lower burst pressure, than compared to higher

Table 9: Advanced abuse model parameters

Parameters	A.Pl	A.Ph	B.Pl	B.Ph	Source/ note
			Abuse sub model		
Wc ($kg\,m^{-3}$)	385.12	385.12	560.24	560.24	estimated, see Table 8
Wp ($kg\,m^{-3}$)	615.26	615.26	977.13	977.13	estimated, see Table 8
We ($kg\,m^{-3}$)			m_e/V_{jelly}		-
$m_{e,0}$ (g)	6.58	6.58	1.95	1.95	estimated, see Table 8
$E_{a,ne}$ ($J\,mol^{-1}$)	1.4183×10^5	1.4042×10^5	1.4751×10^5	1.4325×10^5	fit
$E_{a,sei}$ ($J\,mol^{-1}$)	1.5007×10^5	1.4413×10^5	1.5453×10^5	1.5007×10^5	fit
$E_{a,pe}$ ($J\,mol^{-1}$)	1.0197×10^5	1.0197×10^5	1.0197×10^5	1.03×10^5	fit
$E_{a,e}$ ($J\,mol^{-1}$)	2.877×10^5	2.877×10^5	2.877×10^5	2.877×10^5	fit
A_{ne} (s^{-1})	2.0×10^{13}	1.75×10^{13}	2.25×10^{13}	1.25×10^{13}	fit
A_{sei} (s^{-1})	1.667×10^{15}	1.667×10^{15}	1.667×10^{15}	1.667×10^{15}	fit
A_{pe} (s^{-1})	1.4×10^8	1.4×10^8	1.2×10^8	1.4×10^8	fit
A_e (s^{-1})	3.598×10^{25}	3.598×10^{25}	5.14×10^{25}	5.14×10^{25}	fit
H_{ne} ($J\,g^{-1}$)	3771	3771	2914	2914	fit
H_{sei} ($J\,g^{-1}$)	578	578	578	578	fit
H_{pe} ($J\,g^{-1}$)	292	292	204	224	fit
H_e ($J\,g^{-1}$)	170	170	164	178	fit
			Venting sub model		
$m_{vented,0}$ (g)	0.8	0.8	0.7	0.7	fit
P_{burst} (kPa)	1224 [a]	2158 [b]	1224 [a]	2158 [b]	[a][38], [b][69]
A_v (m^2)			8.9×10^{-6}		[69]
γ (-)			1.4		[38]
k_b ($J\,K^{-1}$)			1.38×10^{-23}		[38]
M_{DMC} ($g\,mol^{-1}$)			90		[38]
M_g ($g\,mol^{-1}$)			44.01		CO_2
$m_{g,rxn}$ (g)			0.88		[31]
P_0 (kPa)			130		[38]
P_{amb} (kPa)			101		[38]
R_{DMC} ($J\,kg^{-1}\,K^{-1}$)			92.38		[38]
R_g ($J\,kg^{-1}\,K^{-1}$)			188.9		CO_2
V_{cell} (m^3)			1.654×10^{-5}		[38]
V_h (m^3)			$0.07*V_{cell}$		[38]
$X_{mixture,0}$ (-)			8.2308×10^{-4}		Calculated from [38]

Table 10: Heat released for different mass compositions and burst pressure scenarios under oven test simulations. (The values in brackets represent the heat released up to the point in time that maximum cell temperature occurs).

	Heat (kJ)							
	Mass composition A				**Mass composition B**			
	T_{oven}=180°C		**T_{oven}=218°C**		**T_{oven}=180°C**		**T_{oven}=218°C**	
	$P_{burst,low}$	**$P_{burst,high}$**	**$P_{burst,low}$**	**$P_{burst,high}$**	**$P_{burst,low}$**	**$P_{burst,high}$**	**$P_{burst,low}$**	**$P_{burst,high}$**
SEI	0.43 (0.43)	0.43 (0.43)	0.43 (0.43)	0.43 (0.43)	0.63 (0.63)	0.63 (0.63)	0.63 (0.63)	0.63 (0.63)
NE	3.09 (2.19)	3.16 (2.26)	7.62 (6.24)	7.56 (6.17)	2.57 (1.65)	2.89 (1.95)	8.07 (6.54)	8.26 (6.73)
PE	1.25 (0.09)	1.14 (0.08)	2.23 (2.23)	2.23 (2.23)	1.07 (0.09)	0.89 (0.08)	2.71 (2.71)	2.71 (2.71)
Electrolyte	0.01 (0.00)	0.00 (0.00)	1.01 (1.01)	1.01 (1.01)	0.00 (0.00)	0.00 (0.00)	0.24 (0.24)	0.24 (0.24)
Simmering	3.57 (0.66)	3.58 (0.70)	4.79 (0.32)	4.81 (0.35)	3.50 (0.78)	3.54 (0.71)	4.76 (0.39)	4.79 (0.36)
Total	**8.34 (3.37)**	**8.31 (3.47)**	**16.06 (10.22)**	**16.04 (10.18)**	**7.76 (3.14)**	**7.95 (3.37)**	**16.41 (10.51)**	**16.64 (10.67)**
Venting	-0.14	-0.13	-0.14	-0.13	-0.12	-0.11	-0.11	-0.10

burst pressures. This can be explained by further looking at the fitted abuse parameters (see Table 9) and the plots of reaction species with time (Fig. 7). By comparing the activation energies of the reactions for the two burst pressure cases (see Table 9), it can be seen that at the higher burst pressure the model requires lowering of the activation energies of the SEI and NE reaction slightly (by 1% to 4%), compared to the lower burst pressure limit. This is due to the fact that, as more gas is required to be generated to meet the higher pressure limit while at the same temperature limit of experimental data, the reaction(s) have to start earlier, as can be seen by the dashed lines in Fig. 7. As the reactions start earlier, so does heat generation, hence higher temperatures are reached sooner, thus making the time to venting shorter but occurring at slightly higher temperatures. This however shows that, by lowering the activation energy of the reactions, the temperature at which venting occurs can be controlled for different assumed burst pressures.

Further, Table 11, presenting the degree of conversion of each reaction just prior to venting, shows that the SEI reaction is the only reaction to undergo a significant degree of conversion, while the NE reaction contributes slightly to the overall decomposition and gas generation. Hence, under the assumption that the mass of gas is dependent on the equal weighting of the four decomposition reactions (see Eq. (3)), gas generation from the SEI and NE reactions are the main contributors to initial gas generation and cell pressurisation up to the cell burst pressure of the experimental results. However, due to the large mass difference between the anode and the SEI it is logical that the NE reaction would produce more gas than the SEI reaction (when fully decomposed). As such, even though the NE reaction is much slower than the SEI it may have a greater influence on gas generation. Hence, it would be beneficial of further work to separate out the gas generation terms for each reaction to identify the amount of gas produced by each reaction through TR.

Considering the large burst pressure range investigated (1224 kPa to 2185 kPa), there is only a small change to the $E_{a,sei}$ and $E_{a,ne}$ parameters, while predictions are almost identical. The value of the burst pressure is therefore not critical to TR model parameterisation. Conversely, if the value of the burst pressure is exactly known, then it would help in parameterisation by requiring that the internal cell pressure is predicted accurately, in addition to the predictions of temperature.

The time to venting is predicted accurately under both oven exposure temperatures and the temperature that venting occurs in the higher oven exposure is accurate (see Fig. 6(c) and Fig. 6(d)). However, the temperature at which venting is predicted in the 180°C oven is noticeably lower than in the experiment. Hence, the discrepancy between the temperature at which venting occurs in the 180°C simulation and experiment highlights that the AAM, while significantly improving predictions, lacks some features that influence the complex pressure behaviour.

Table 12 also shows the ratio of gas generation between the high and low burst limit simulation, from which, at the higher burst limit three times more gas is produced prior to venting. Also, the magnitude of gas generated prior to

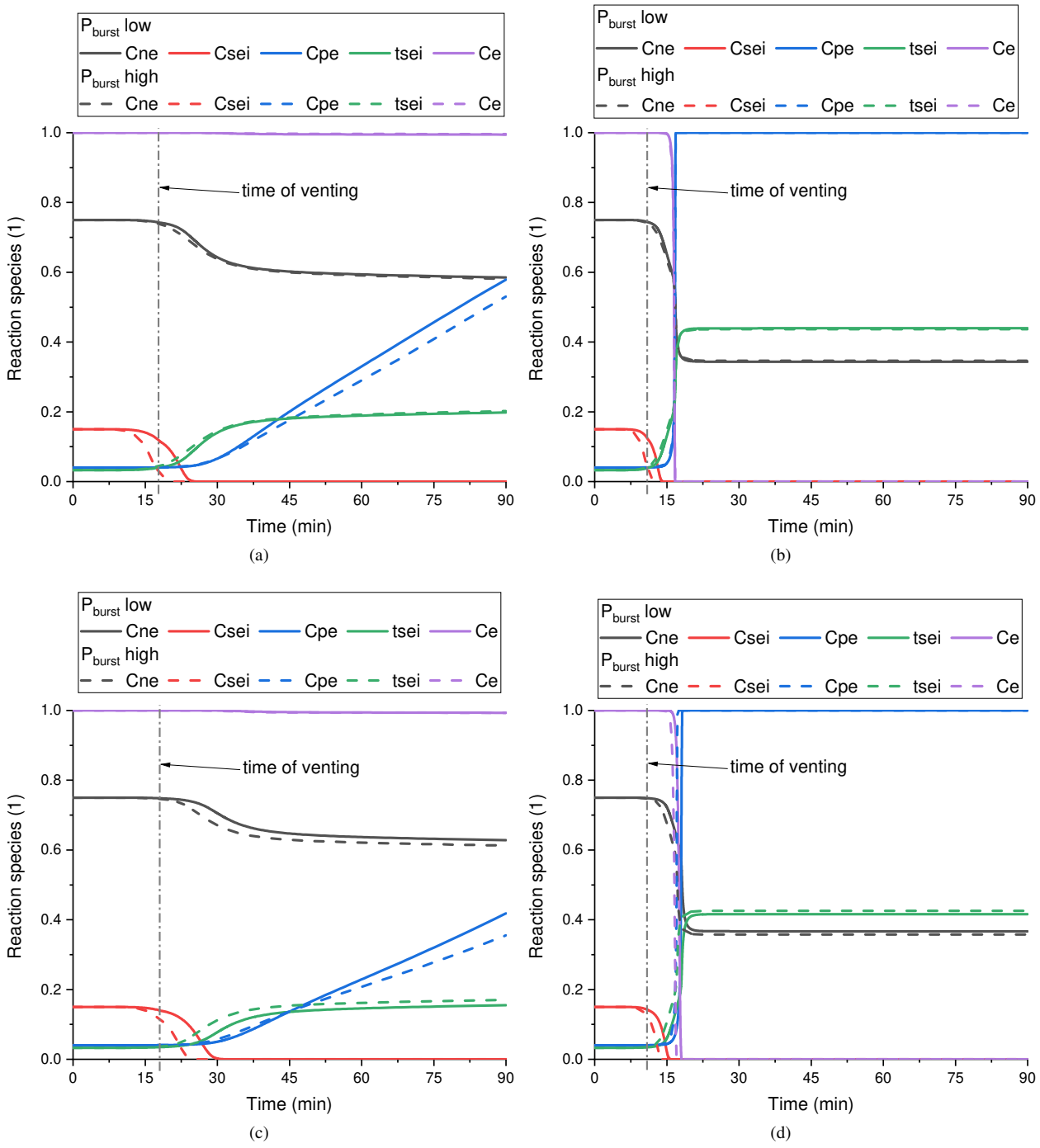

Figure 7: Plots of the cell decomposition species vs. time at different oven temperature, cell mass compositions and burst pressure limits. Sub-figures: (a) oven at 180°C, mass composition A; (b) oven at 218°C, mass composition A; (c) oven at 180°C, mass composition B; (d) oven at 218°C, mass composition B, for high and low burst pressures. Time of venting is average of both the high and low burst cases (as, on the time scale shown, individual lines for each pressure limit are indistinguishable).

Table 11: Percentage degree of conversion for each reaction at the point just prior to venting for different mass compositions and burst pressure scenarios.

	Degree of conversion (%)							
	Mass composition A				**Mass composition B**			
	T_{oven}=180°C		**T_{oven}=218°C**		**T_{oven}=180°C**		**T_{oven}=218°C**	
	$P_{burst,low}$	**$P_{burst,high}$**	**$P_{burst,low}$**	**$P_{burst,high}$**	**$P_{burst,low}$**	**$P_{burst,high}$**	**$P_{burst,low}$**	**$P_{burst,high}$**
C_{sei}	23.87	72.79	19.95	66.17	7.50	22.34	6.25	20.24
C_{ne}	1.07	1.24	0.87	1.10	0.27	0.45	0.22	0.40
C_{pe}	0.07	0.06	0.05	0.05	0.06	0.05	0.04	0.04
C_e	0.00	0.00	0.00	0.00	0.00	0.00	0.00	0.00

Table 12: Amount of gas generated and average decomposition of cell at the instant before venting.

Mass composition at oven set temperature	**P_b=1224 kPa**		**P_b=2158 kPa**		**Mass ratio**
	m_g (g) $\times 10^{-2}$	**C_{ave} (-)**	**m_g (g) $\times 10^{-2}$**	**C_{ave} (-)**	
A, 180°C	5.76	0.9375	16.6	0.8148	2.88
B, 180°C	1.80	0.9804	5.10	0.9429	2.83
A, 218°C	4.85	0.9478	15.1	0.8317	3.11
B, 218°C	1.51	0.9837	4.63	0.9483	3.07

venting is on the order of, or two orders lower, that the total measured, e.g 0.79 g to 1.4 g [12, 31, 32], depending on the assumed burst pressure.

A possible cause of discrepancy in venting temperature is the lack of calculation of the overall vapour/ liquid ratio of the mixture and the lack of calculation of the composition (i.e. CO_2/DMC ratio) of the liquid and vapour phases. As for dissimilar fluids, like the case for CO_2/DMC here, the mole fraction of each phase can be very different as the data in Ref. [64] shows. Hence, the bulk mole fraction assumption used here for simplicity (which is acceptable for fluids that are very similar to each other) may be inaccurate for a complete description of venting. However, for the purpose of validating the BPV model as a way to govern internal pressure rather than using the PPV model, we believe it is acceptable for proving that new model is valid, while further work beyond the scope of this paper is required to incorporate the compositions of each phase

3.4. Validation

Further validation of the estimated parameters for the AAM can be achieved by simulating the oven experiment over a range of values below and above those so far discussed. Figure 8 is a plot of the maximum cell temperature, and maximum change in cell temperature compared to the oven set temperature, against the oven set temperature, for experimental and computational results. From Fig. 8 it is clear the model predictions are in good agreement with the experimental data. Hence, the model can be used to investigate cell abuse beyond the experimental temperature range. However, from Fig. 8, over the range that experimental data is presented, the predicted temperatures are

somewhat lower at oven set temperatures below 180°C and between 195°C–205°C. At the critical point at 195°C, where there is a step change in the TR severity of the experimental data, the model predicts the step change but does not predict the correct magnitude of temperature increase. Below is discussed possible contributing factors that lead to the discrepancies in predictions of Fig. 8.

The under prediction of maximum cell surface temperature at oven set temperatures below 180°C in Fig. 8 are attributed to, as previously discussed in Section 3.3, a lack of representation of additional reactions. The discrepancies at oven set temperatures of 195°C–205°C are thought to be linked to the under prediction of step change at the oven set temperature of 195°C. The suspected additional reactions not accounted for, may, at higher temperatures contribute to the sudden increase in reactivity at 195°C. Further, electrolyte combustion in the presence of O_2 [3, 22], from O_2 released on cathode decomposition [49], is a likely cause considering the step change occurs at surface temperatures within the PE decomposition range, see Table 1. Further investigation, beyond the scope of this work, would be required to identify additional reactions.

The model allows assessment of TR behaviour beyond the scope of experimental testing. At an oven set temperature of 140°C the maximum cell temperature is equal to that of the oven set temperature. Hence, from these predictions the LFP cells in question are shown to be stable up to 140°C oven exposure. From 140°C to 185°C oven set temperature, there is a steady increase in severity, following a linear trend, that, on the whole, is small, i.e ΔT below 50°C. Between 185°C and 220°C oven set temperature, there is a significant increase in severity, with ΔT equal to 150°C at 218°C oven set temperature. Most interestingly, however, beyond an oven set temperature of 218°C, there is little increase in severity in relative terms to the oven set temperature; in fact, beyond 230°C, there is a slight decrease in relative severity.

As such, the use of this AAM has enabled the prediction of the severity outside the experimental range. Showing that cells abused beyond 190°C lead to a similar hazard regardless of oven set temperature. Further, if cells are kept below 185°C, where the PE and electrolyte reactions are avoided, then the hazard a cell poses is small. A hazard on this scale would be manageable by traditional thermal management techniques for battery packs, considering the maximum heat generated at this abuse temperature is under 5 W, which is on the scale of the heat generated (up to 2.6 W [74]) by a high rate discharge of a similar cell.

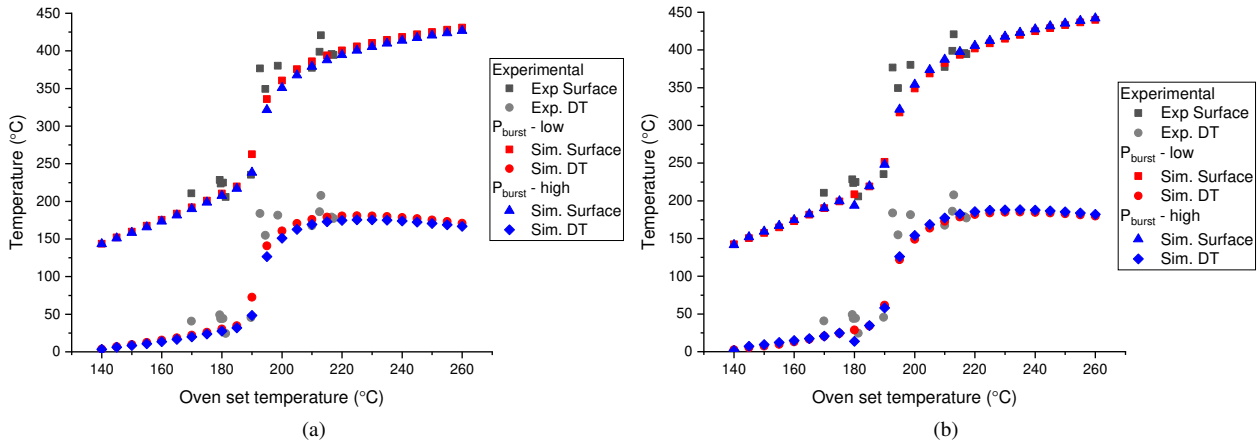

Figure 8: Simulated thermal runaway severity vs oven abuse temperature (a) mass composition A (b) mass composition B, compared to experimental data.

4. Conclusion

The work here develops an AAM to address the inadequate performance of current TR models for Li-ion cells, while highlighting the inappropriateness of abuse parameter values within the literature leading to the necessity of parameter estimation.

The AAM model outperforms classical TR models due to its inclusion of novel venting behaviour and simmering reactions. The venting behaviour, based on a bubble-point assumption, is a more accurate description of a multiphase, multicomponent, system like a cell under TR. The AAM leads to accurate predictions of time to venting, magnitude of heat loss at venting and time to maximum TR temperature. The inclusion of simmering reactions improves predictions of temperature after a TR, and hence is essential for LFP cells.

Accurate knowledge of the burst pressure is required for determining accurate reaction parameters. For higher burst pressures, the activation energies for the SEI and the NE reactions must be reduced, to allow the pressure increase by the time that venting should occur. The time of venting is most dependent on the decomposition of the SEI reaction, and slightly on the NE reaction.

The work here aids the wider LIB community and the development of advanced batteries. The AAM, with its predictions of internal cell pressure, is a development enabling two pressure dependent phenomena to be modelled. The first, the prediction of battery state-of-health through pressure sensors in state-of-the-art battery management systems. The second, the modelling of the ejecta process and with it the complex heat transfer process of ejecta flow in a battery pack.

Three points are outlined for future work regarding the development of LIB TR models:

1. consideration of secondary and interdependent reactions;

2. improved phase-equilibria of the liquid-vapour mixture, i.e. accounting for the liquid-vapour fraction and mole fraction in each phase, expansion of vapour phase and re-equilibrium, improving pressure predictions during venting; and

3. focus on developing an intelligent computational aided method for model parameterisation, enabling statistical analysis of the appropriateness of parameters values.

Conflicts of interest

There are no conflicts to declare.

Acknowledgements

The authors gratefully acknowledge the financial support of the Engineering and Physical Sciences Research Council (EPSRC) in the form of the Energy Storage and its Applications Centre for Doctoral Training (EP/L016818/1).

References

[1] T.-H. Kim, J.-S. Park, S. K. Chang, S. Choi, J. H. Ryu, H.-K. Song, The Current Move of Lithium Ion Batteries Towards the Next Phase, Advanced Energy Materials 2 (7) (2012) 860–872. doi:10.1002/aenm.201200028.

[2] T. Placke, R. Kloepsch, S. Dühnen, M. Winter, Lithium ion, lithium metal, and alternative rechargeable battery technologies: the odyssey for high energy density, Journal of Solid State Electrochemistry 21 (7) (2017) 1939–1964. doi:10.1007/s10008-017-3610-7.

[3] Q. Wang, P. Ping, X. Zhao, G. Chu, J. Sun, C. Chen, Thermal runaway caused fire and explosion of lithium ion battery, Journal of Power Sources 208 (2012) 210–224. doi:10.1016/j.jpowsour.2012.02.038.

[4] D. Lisbona, T. Snee, A review of hazards associated with primary lithium and lithium-ion batteries, Process Safety and Environmental Protection 89 (6) (2011) 434–442. doi:10.1016/j.psep.2011.06.022.

[5] T. Ohsaki, T. Kishi, T. Kuboki, N. Takami, N. Shimura, Y. Sato, M. Sekino, A. Satoh, Overcharge reaction of lithium-ion batteries, Journal of Power Sources 146 (1-2) (2005) 97–100. doi:10.1016/j.jpowsour.2005.03.105.

[6] H. Huo, Y. Xing, M. Pecht, B. J. Züger, N. Khare, A. Vezzini, Safety Requirements for Transportation of Lithium Batteries, Energies 10 (6) (2017) 793–829. doi:10.3390/en10060793.

[7] V. Ruiz, A. Pfrang, A. Kriston, N. Omar, P. V. D. Bossche, L. Boon-Brett, A review of international abuse testing standards and regulations for lithium ion batteries in electric and hybrid electric vehicles, Renewable and Sustainable Energy Reviews 81 (2018) 1427–1452. doi:10.1016/j.rser.2017.05.195.

[8] H. U. Escobar-Hernandez, R. M. Gustafson, M. I. Papadaki, S. Sachdeva, M. S. Mannan, Thermal Runaway in Lithium-Ion Batteries: Incidents, Kinetics of the Runaway and Assessment of Factors Affecting Its Initiation, Journal of The Electrochemical Society 163 (13) (2016) A2691–A2701. doi:10.1149/2.0921613jes.

[9] K. Bullis, Are Electric Vehicles a Fire Hazard?, [online] Available at: https://www.technologyreview.com/s/521976/are-electric-vehicles-a-fire-hazard/ [Accessed 18 August 2017] (2013).

[10] R. Campbell, Electronic Cigarette Explosions and Fires: The 2015 Experience, Tech. rep., [online] Available at: http://www.nfpa.org/news-and-research/fire-statistics-and-reports/fire-statistics/fire-causes/

electrical-and-consumer-electronics/electronic-cigarette-explosions-and-fires-the-2015-experience [Accessed 18 August 2017] (2016).

[11] S. Hollister, Here are the reasons why so many hoverboards are catching fire, [online] Available at: https://www.cnet.com/uk/news/why-are-hoverboards-exploding-and-catching-fire/ [Accessed 18 August 2017] (2016).

[12] A. W. Golubkov, D. Fuchs, J. Wagner, H. Wiltsche, C. Stangl, G. Fauler, G. Voitic, A. Thaler, V. Hacker, Thermal-runaway experiments on consumer Li-ion batteries with metal-oxide and olivin-type cathodes, RSC Advances (4) (2014) 3633–3642. doi:10.1039/c3ra45748f.

[13] J. Jiang, J. R. Dahn, ARC studies of the thermal stability of three different cathode materials: $LiCoO_2$; $Li[Ni_{0.1}Co_{0.8}Mn_{0.1}]O_2$; and $LiFePO_4$, in $LiPF_6$ and LiBoB EC/DEC electrolytes, Electrochemistry Communications 6 (1) (2004) 39–43. doi:10.1016/j.elecom.2003.10.011.

[14] X. Liu, Z. Wu, S. I. Stoliarov, M. Denlinger, A. Masias, K. Snyder, Heat release during thermally-induced failure of a lithium ion battery: Impact of cathode composition, Fire Safety Journal 85 (2016) 10–22. doi:10.1016/j.firesaf.2016.08.001.

[15] OFweek, [Shenzhen Wuzhoulong electric bus burning and explosion, BYD issued an announcement to clarify], [online] Available at: http://nev.ofweek.com/2015-04/ART-71008-8120-28951921.html [Accessed 19 September 2018] (In Chinese) (2015).

[16] B. Lei, W. Zhao, C. Ziebert, N. Uhlmann, M. Rohde, H. Seifert, Experimental Analysis of Thermal Runaway in 18650 Cylindrical Li-Ion Cells Using an Accelerating Rate Calorimeter, Batteries 3 (2) (2017) 14. doi:10.3390/batteries3020014.

[17] F. Larsson, B.-E. Mellander, Abuse by External Heating , Overcharge and Short Circuiting of Commercial Lithium-Ion Battery Cells, Journal of The Electrochemical Society 161 (10) (2014) A1611–A1617. doi:10.1149/2.0311410jes.

[18] X. Feng, M. Ouyang, X. Liu, L. Lu, Y. Xia, X. He, Thermal runaway mechanism of lithium ion battery for electric vehicles: A review, Energy Storage Materials 10 (2018) 246–267. doi:10.1016/j.ensm.2017.05.013.

[19] D. Doughty, E. P. Roth, A General Discussion of Li Ion Battery Safety, The Electrochemical Society Interface 21 (2) (2012) 37–44.

[20] G. H. Kim, A. Pesaran, R. Spotnitz, A three-dimensional thermal abuse model for lithium-ion cells, Journal of Power Sources 170 (2) (2007) 476–489. doi:10.1016/j.jpowsour.2007.04.018.

[21] T. D. Hatchard, D. D. MacNeil, A. Basu, J. R. Dahn, Thermal Model of Cylindrical and Prismatic Lithium-Ion Cells, Journal of The Electrochemical Society 148 (7) (2001) A755–A761. doi:10.1149/1.1377592.

[22] C. F. Lopez, J. A. Jeevarajan, P. P. Mukherjee, Characterization of Lithium-Ion Battery Thermal Abuse Behavior Using Experimental and Computational Analysis, Journal of The Electrochemical Society 162 (10) (2015) A2163–A2173. doi:10.1149/2.0751510jes.

[23] P. Peng, F. Jiang, Thermal safety of lithium-ion batteries with various cathode materials: A numerical study, International Journal of Heat and Mass Transfer 103 (2016) 1008–1016. doi:10.1016/j.ijheatmasstransfer.2016.07.088.

[24] G. Guo, B. Long, B. Cheng, S. Zhou, P. Xu, B. Cao, Three-dimensional thermal finite element modelling of lithium-ion battery in thermal abuse application, Journal of Power Sources 195 (8) (2010) 2393–2398. doi:10.1016/j.jpowsour.2009.10.090.

[25] S. Abada, M. Petit, A. Lecocq, G. Marlair, V. Sauvant-Moynot, F. Huet, Combined experimental and modeling approaches of the thermal runaway of fresh and aged lithium-ion batteries, Journal of Power Sources 399 (2018) 264 – 273. doi:https://doi.org/10.1016/j.jpowsour.2018.07.094.
URL http://www.sciencedirect.com/science/article/pii/S037877531830819X

[26] R. Spotnitz, J. Franklin, Abuse behavior of high-power, lithium-ion cells, Journal of Power Sources 113 (1) (2003) 81–100.

[27] P. T. Coman, E. C. Darcy, C. T. Veje, R. E. White, Modelling Li-Ion Cell Thermal Runaway Triggered by an Internal Short Circuit Device Using an Efficiency Factor and Arrhenius Formulations, Journal of The Electrochemical Society 164 (4) (2017) A587–A593. doi:10.1149/2.0341704jes.

[28] K.-C. Chiu, C.-H. Lin, S.-F. Yeh, Y.-H. Lin, K.-C. Chen, An electrochemical modelling of lithium-ion battery nail penetration, Journal of Power Sources 251 (2014) 254–263. doi:10.1016/j.jpowsour.2013.11.069.
URL http://dx.doi.org/10.1016/j.jpowsour.2013.11.069

[29] P. J. Bugryniec, J. N. Davidson, D. J. Cumming, S. F. Brown, Pursuing safer batteries: Thermal abuse of $LiFePO_4$ cells, Journal of Power Sources 414 (2019) 557–568. doi:10.1016/j.jpowsour.2019.01.013.

[30] A. Melcher, C. Ziebert, M. Rohde, H. J. Seifert, Modeling and simulation of the thermal runaway behavior of cylindrical Li-ion cells-computing of critical parameters, Energies 9 (4) (2016) 1–19. doi:10.3390/en9040292.

[31] A. W. Golubkov, S. Scheikl, R. Planteu, G. Voitic, H. Wiltsche, C. Stangl, G. Fauler, A. Thaler, V. Hacker, Thermal runaway of commercial 18650 Li-ion batteries with LFP and NCA cathodes - impact of state of charge and overcharge, RSC Adv. 5 (70) (2015) 57171–57186. doi:10.1039/C5RA05897J.

[32] Y. Fernandes, A. Bry, S. de Persis, Identification and quantification of gases emitted during abuse tests by overcharge of a commercial li-ion battery, Journal of Power Sources 389 (2018) 106 – 119. doi:https://doi.org/10.1016/j.jpowsour.2018.03.034.
URL http://www.sciencedirect.com/science/article/pii/S0378775318302581

[33] P. T. Coman, S. Rayman, R. E. White, A lumped model of venting during thermal runaway in a cylindrical Lithium Cobalt Oxide lithium-ion cell, Journal of Power Sources 307 (2016) 56–62. doi:10.1016/j.jpowsour.2015.12.088.

[34] C. H. Lee, S. J. Bae, M. Jang, A study on effect of lithium ion battery design variables upon features of thermal-runaway using mathematical model and simulation, Journal of Power Sources 293 (2015) 498–510. doi:10.1016/j.jpowsour.2015.05.095.

[35] P. Ping, Q. Wang, Y. Chung, J. Wen, Modelling electro-thermal response of lithium-ion batteries from normal to abuse conditions, Applied Energy 205 (2017) 1327–1344. doi:10.1016/j.apenergy.2017.08.073.

[36] T. Dong, P. Peng, F. Jiang, Numerical modeling and analysis of the thermal behavior of NCM lithium-ion batteries subjected to very high C-rate discharge/charge operations, International Journal of Heat and Mass Transfer 117 (2018) 261–272. doi:10.1016/j.ijheatmasstransfer.2017.10.024.

[37] S. Wang, L. Lu, X. Liu, A simulation on safety of $LiFePO_4$/C cell using electrochemical-thermal coupling model, Journal of Power Sources 244 (2013) 101–108. doi:10.1016/j.jpowsour.2013.03.100.

[38] P. T. Coman, M. Stefan, C. T. Veje, R. E. White, Modeling Vaporization, Gas Generation and Venting in Li-Ion Battery Cells with a Dimethyl Carbonate Electrolyte, Journal of The Electrochemical Society 164 (9) (2017) 1858–1865. doi:10.1149/2.0631709jes.

[39] E. P. Roth, D. H. Doughty, Thermal abuse performance of high-power 18650 Li-ion cells, Journal of Power Sources 128 (2) (2004) 308–318. doi:10.1016/j.jpowsour.2003.09.068.

[40] D. P. Abraham, E. P. Roth, R. Kostecki, K. McCarthy, S. MacLaren, D. H. Doughty, Diagnostic examination of thermally abused high-power lithium-ion cells, Journal of Power Sources 161 (1) (2006) 648–657. doi:10.1016/j.jpowsour.2006.04.088.

[41] M. N. Richard, J. R. Dahn, Accelerating Rate Calorimetry Study on the Thermal Stability of Lithium Intercalated Graphite in Electrolyte. II. Modeling the Results and Predicting Differential Scanning Calorimeter Curves, Journal of The Electrochemical Society 146 (6) (1999) 2078–2084. doi:10.1149/1.1391894.

[42] D. D. MacNeil, L. Christensen, J. Landucci, J. M. Paulsen, J. R. Dahn, An Autocatalytic Mechanism for the Reaction of Li_xCoO_2 in Electrolyte at Elevated Temperature, Journal of The Electrochemical Society 147 (3) (2000) 970–979. doi:10.1149/1.1393299.

[43] I. Belharouak, Y.-K. Sun, W. Lu, K. Amine, On the Safety of the $Li_4Ti_5O_{12}$\$LiMn_2O_4$ Lithium-Ion Battery System, Journal of The Electrochemical Society 154 (12) (2007) A1083. doi:10.1149/1.2783770.

[44] A. Ben Mayza, M. Ramanathan, R. Radhakrishnan, S. Ha, V. Ramani, J. Prakash, K. Zaghib, Thermal Characterization of $LiFePO_4$ Cathode in Lithium Ion Cells, ECS Transactions 35 (34) (2011) 177–183.

[45] A. Yamada, S. C. Chung, K. Hinokuma, Optimized $LiFePO_4$ for Lithium Battery Cathodes, Journal of Electroanalytical Society 148 (3) (2001) 224–229. doi:10.1149/1.1348257.

[46] D. D. MacNeil, Z. Lu, Z. Chen, J. R. Dahn, A comparison of the electrode/electrolyte reaction at elevated temperatures for various Li-ion battery cathodes, Journal of Power Sources 108 (1-2) (2002) 8–14.

[47] M. Takahashi, S.-i. Tobishima, K. Takei, Y. Sakurai, Reaction behavior of $LiFePO_4$ as a cathode material for rechargeable lithium batteries, Solid State Ionics 148 (3-4) (2002) 283–289.

[48] J. Jiang, J. R. Dahn, ARC studies of the reaction between $LiFePO_4$ and $LiPF_6$ or LiBOB EC/DEC electrolytes, Electrochemistry Communications 6 (7) (2004) 724–728. doi:10.1016/j.elecom.2004.05.004.

[49] G. Chen, T. J. Richardson, Thermal instability of Olivine-type $LiMnPO_4$ cathodes, Journal of Power Sources 195 (4) (2010) 1221–1224. doi:10.1016/j.jpowsour.2009.08.046.

[50] D. Ren, X. Liu, X. Feng, L. Lu, M. Ouyang, J. Li, X. He, Model-based thermal runaway prediction of lithium-ion batteries from kinetics analysis of cell components, Applied Energy 228 (2018) 633–644. doi:10.1016/j.apenergy.2018.06.126.

[51] A. Kvasha, C. Gutiérrez, U. Osa, I. de Meatza, J. A. Blazquez, H. Macicior, I. Urdampilleta, A comparative study of thermal runaway of commercial lithium ion cells, Energy 159 (2018) 547 – 557. doi:https://doi.org/10.1016/j.energy.2018.06.173.

[52] D. D. MacNeil, T. D. Hatchard, J. R. Dahn, A Comparison Between the High Temperature Electrode/Electrolyte Reactions of Li_xCoO_2 and $Li_xMn_2O_4$, Journal of The Electrochemical Society 148 (7) (2001) A663–A667. doi:10.1149/1.1375798.

[53] Q. Li, C. Yang, S. Santhanagopalan, K. Smith, J. Lamb, L. A. Steele, L. Torres-Castro, Numerical investigation of thermal runaway mitigation through a passive thermal management system, Journal of Power Sources 429 (2019) 80 – 88. doi:https://doi.org/10.1016/j.jpowsour.2019.04.091.
URL http://www.sciencedirect.com/science/article/pii/S0378775319305026

[54] Z. An, K. Shah, L. Jia, Y. Ma, Modeling and analysis of thermal runaway in li-ion cell, Applied Thermal Engineering 160 (2019) 113960. doi:https://doi.org/10.1016/j.applthermaleng.2019.113960.
URL http://www.sciencedirect.com/science/article/pii/S135943111837786X

[55] R. M. Felder, R. W. Rousseau, Elementary Principles of Chemical Processes, 3rd Edition, John Wiley & Sons, Inc., 2005.

[56] P. Ping, Q. Wang, P. Huang, J. Sun, C. Chen, Thermal behaviour analysis of lithium-ion battery at elevated temperature using deconvolution method, Applied Energy 129 (2014) 261–273. doi:10.1016/j.apenergy.2014.04.092.

[57] D. H. Doughty, P. C. Butler, R. G. Jungst, E. P. Roth, Lithium battery thermal models, Journal of Power Sources 110 (2) (2002) 357–363. doi:10.1016/S0378-7753(02)00198-2.

[58] M. N. Richard, J. R. Dahn, Accelerating Rate Calorimetry Study on the Thermal Stability of Lithium Intercalated Graphite in Electrolyte I. Experimental, Journal of The Electrochemical Society 146 (6) (1999) 2068–2077. doi:10.1149/1.1391894.

[59] D. D. Macneil, J. R. Dahn, Test of Reaction Kinetics Using Both Differential Scanning and Accelerating Rate Calorimetries As Applied to the Reaction of Li_xCoO_2 in Non-aqueous Electrolyte, The Journal of Physical Chemistry A 105 (18) (2001) 4430–4439. doi:10.1021/jp001187j.

[60] Y. Nishiyama, T. Tanaka, K. Nakajima, Numerical simulations of thermal behavior in relation with safety improvement of li-ion battery, ECS Meeting Abstracts MA2006-02 (5) (2006) 329. arXiv:http://ma.ecsdl.org/content/MA2006-02/5/329.full.pdf+html.

[61] R. Milton, P. Bugryniec, S. Brown, Parameter estimation for thermal runaway of li-ion cells: a gaussian process approach, in: A. A. Kiss, E. Zondervan, R. Lakerveld, L. Özkan (Eds.), 29th European Symposium on Computer Aided Process Engineering, Vol. 46 of Computer Aided Chemical Engineering, Elsevier, 2019, pp. 775 – 780. doi:https://doi.org/10.1016/B978-0-12-818634-3.

50130-2.

URL http://www.sciencedirect.com/science/article/pii/B9780128186343501302

[62] R. Curtis, J. Martin, D. Cao, Zero-Order Reactions, [online] Available at: https://chem.libretexts.org/Bookshelves/Physical_and_Theoretical_Chemistry_Textbook_Maps/Supplemental_Modules_(Physical_and_Theoretical_Chemistry)/Kinetics/Reaction_Rates/Zero-Order_Reactions [Accessed 11 October 2019] (Sep. 2019).

[63] X. Feng, S. Zheng, D. Ren, X. He, L. Wang, H. Cui, X. Liu, C. Jin, F. Zhang, C. Xu, H. Hsu, S. Gao, T. Chen, Y. Li, T. Wang, H. Wang, M. Li, M. Ouyang, Investigating the thermal runaway mechanisms of lithium-ion batteries based on thermal analysis database, Applied Energy 246 (2019) 53 – 64. doi:https://doi.org/10.1016/j.apenergy.2019.04.009.

URL http://www.sciencedirect.com/science/article/pii/S0306261919306348

[64] E. W. Lemmon, I. H. Bell, M. L. Huber, M. O. McLinden, NIST Standard Reference Database 23: Reference Fluid Thermodynamic and Transport Properties-REFPROP, Version 10.0, National Institute of Standards and Technology (2018).

[65] R. Akasaka, T. Yamaguchi, T. Ito, Practical and direct expressions of the heat of vaporization for mixtures, Chemical Energy Science 60 (2005) 4369–4376. doi:10.1016/j.ces.2005.03.005.

[66] COMSOL Multiphysics®V5.2a, www.comsol.com. COMSOL AB, Stockholm, Sweden.

[67] L. H. Saw, Y. Ye, A. A. O. Tay, Electrochemical – thermal analysis of 18650 Lithium Iron Phosphate cell, Energy Conversion and Management 75 (2013) 162–174. doi:10.1016/j.enconman.2013.05.040.

[68] B. Streipert, K. Krämer, L. Terborg, V. Kraft, J. Menzel, D. Gallus, I. Cekic-Laskovic, S. Nowak, T. Placke, M. Winter, Vernachlässigt, vergessen oder unwichtig? - Inaktivmaterialien für Lithium-Ionen Batterien, [online] Available at: https://www.gdch.de/fileadmin/downloads/Netzwerk_und_Strukturen/Fachgruppen/Seniorexperten/PDF/Tagungen/6_SEC_Jahrestreffen/Winter02.pdf [accessed 22 March 2019] (2016).

[69] F. A. Mier, M. J. Hargather, S. R. Ferreira, Experimental Quantification of Vent Mechanism Flow Parameters in 18650 Format Lithium Ion Batteries, Journal of Fluids Engineering 141 (6) (2019) 061403-1–061403-11. doi:10.1115/1.4042962.

[70] F. L. H. Rajiwate, Investigation of Compressible Fluid Behaviour in a Vent Pipe during Blowdown, Ph.D. thesis, Curtin University (2011).

[71] S. Brown, S. Martynov, H. Mahgerefteh, S. Chen, Y. Zhang, Modelling the non-equilibrium two-phase flow during depressurisation of co2 pipelines, International Journal of Greenhouse Gas Control 30 (2014) 9 – 18. doi:https://doi.org/10.1016/j.ijggc.2014.08.013.

URL http://www.sciencedirect.com/science/article/pii/S1750583614002394

[72] A. M. Haregewoin, A. S. Wotango, B.-J. Hwang, Electrolyte additives for lithium ion battery electrodes: progress and perspectives, Energy & Environmental Science 9 (2016) 1955–1988. doi:10.1039/C6EE00123H.

URL https://pubs.rsc.org/en/content/articlelanding/2016/EE/C6EE00123H#!divAbstract

[73] P. Sehrawat, C. Julien, S. Islam, Carbon nanotubes in Li-ion batteries: A review, Materials Science and Engineering: B 213 (2016) 12 – 40, li-ion batteries. doi:https://doi.org/10.1016/j.mseb.2016.06.013.

URL http://www.sciencedirect.com/science/article/pii/S0921510716300873

[74] T. M. Bandhauer, S. Garimella, T. F. Fuller, Temperature-dependent electrochemical heat generation in a commercial lithium-ion battery, Journal of Power Sources 247 (2014) 618 – 628. doi:https://doi.org/10.1016/j.jpowsour.2013.08.015.

URL http://www.sciencedirect.com/science/article/pii/S0378775313013530